Canard- and Hopf-Induced Bursting in Pituitary Cells

Theodore Vo

These are notes for the talk given at the BU/Keio Dynamical Systems workshop (September 19, 2014) at Boston University. These notes are heavily inspired by [11].

Abstract

It has been shown that large conductance potassium (BK) current tends to promote bursting in pituitary cells. This requires fast activation of the BK current, otherwise it is inhibitory to bursting. In this work we combine theoretical (geometric singular perturbation theory), experimental (dynamic clamp) and numerical (AUTO) methods to understand why the BK activation must be fast in order to promote bursting.

1 Introduction

The electrical activity of pituitary cells regulates diverse functional characteristics such as the release of prolactin, growth hormone and ACTH in lactotrophs, somatotrophs and corticotrophs, respectively. One pattern of electrical activity commonly seen in pituitary cells is *pseudo-plateau bursting*, which consists of alternating periods of small-amplitude oscillations (SAOs) in the active (depolarized) phase followed by silent phases during which repolarization occurs (Figure 1(a)).

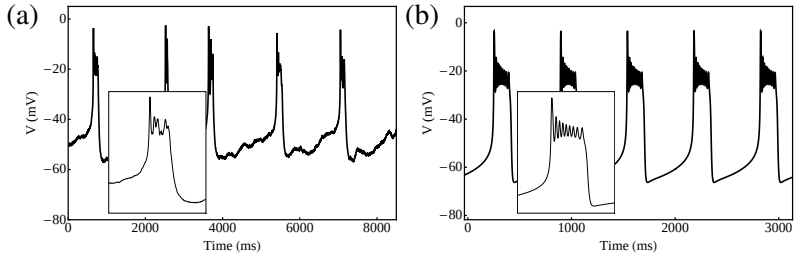

Figure 1: Pseudo-plateau bursting (a) recorded in an unstimulated GH4C1 lacto-somatotroph cell line and (b) generated by a deterministic mathematical model. Insets: magnified view of a single burst.

Pituitary cells express a variety of ion channels and establishing the role of any given channel type is difficult. One example where the function of the ion channel is clear is the role of large conductance potassium (BK) channels in the spiking/bursting activity of pituitary cells [8]. In [10], it was demonstrated experimentally that fast-activating BK channels promote bursting in pituitary cells. The primary aim of this work is to understand why BK activation must be fast to promote bursting.

Two common mechanisms for bursting are canard dynamics and slow passage through a dynamic Hopf bifurcation [2]. In these notes, we analyze a pituitary cell model and show that both canard and Hopf mechanisms are possible, depending on parameter values. We then describe the dynamic clamp experiments that were performed to test our theoretical predictions.

2 The Mathematical Model

We consider a mathematical model that provides a minimal description of the electrical activity and calcium dynamics in pituitary cells [10]. There are three voltage-gated currents (I_{Ca}, I_{BK}, I_K), a calcium-gated current, I_{SK}, and a leak current, I_L. The state variables are the membrane potential V

of the cell, activation variables n and b for the K and BK channels, respectively, and the intracellular calcium concentration c. Their dynamics are governed by the evolution equations

$$\begin{aligned} C_m \frac{dV}{dt} &= -(I_{Ca} + I_{BK} + I_K + I_{SK} + I_L), \\ \tau_{BK} \frac{db}{dt} &= b_\infty(V) - b, \\ \tau_n \frac{dn}{dt} &= n_\infty(V) - n, \\ \frac{dc}{dt} &= -f_c(\alpha I_{Ca} + k_c c), \end{aligned} \tag{1}$$

where the ionic currents are given by

$$I_{Ca} = g_{Ca} m_\infty(V)(V - V_{Ca}), \qquad I_{BK} = g_{BK} b(V - V_K), \qquad I_K = g_K n(V - V_K),$$
$$I_{SK} = g_{SK} s_\infty(c)(V - V_K), \qquad I_L = g_L(V - V_L),$$

and the steady state functions are given by

$$x_\infty(V) = \left[1 + \exp\left(\frac{V_x - V}{s_x}\right)\right]^{-1}, \qquad s_\infty(c) = \frac{c^2}{c^2 + k_s^2},$$

where $x \in \{m, b, n\}$. Standard parameter values are listed in Table 1. All parameters are set at these standard values unless stated otherwise.

C_m	$0 - 10$ pF	g_{Ca}	2 nS	V_{Ca}	60 mV	V_m	-20 mV	s_m	12 mV
g_K	1.5 nS	V_K	-75 mV	V_n	-5 mV	s_n	10 mV	τ_n	30 ms
g_{SK}	2 nS	k_s	0.4 μM	g_{BK}	$0 - 1$ nS	V_b	-20 mV	s_b	2 mV
τ_{BK}	$2 - 10$ ms	g_L	0.2 nS	V_L	-50 mV	f_c	0.01	α	0.0015 μMfC^{-1}
k_c	0.12 ms^{-1}								

Table 1: Standard parameter values for the 4D pituitary cell model

2.1 Fast-Activating BK Channels Promote Bursting

Using AUTO [3], the bifurcation structure of (1) was calculated with τ_{BK} as the principal continuation parameter (Figure 2(g)). For large τ_{BK} (i.e. slow activation), the system is spiking (panel (a)). As τ_{BK} is decreased, the system generates bursts (panels (b)–(d)), which have sensitive dependence to τ_{BK}. Decreasing τ_{BK} rapidly increases the number of SAOs and decreases their amplitude. For sufficiently small τ_{BK}, we observe damped oscillations followed by a plateau in the active phase (panel (e)). Further decreases in τ_{BK} only intensify the damping effect and the oscillatory behaviour gives way to a flat plateau (panel (f)).

The time traces in Figure 2 show that the amplitude and number of small oscillations in the bursts changes very rapidly under τ_{BK} variations. Changes in the other system parameters however can alter the bifurcation structure. Figure 3(e) shows an example of how a change in g_{BK} dramatically alters the bifurcation structure of (1). The number and amplitude of the SAOs in the bursting rhythms for this parameter set have little variation under τ_{BK} variations.

Figures 2 and 3 hint at the notion that (in addition to τ_{BK}) g_{BK} is a crucial factor in shaping the electrical activity. In [11], simulations show that there exists some kind of threshold conductance that divides the system into 2 kinds of behaviour. Above threshold, the system exhibits extreme sensitivity to τ_{BK}. Below threshold, the system is virtually insensitive to τ_{BK}. This suggests that the mechanism that generates the bursts is somehow different above and below threshold. We would like to understand why in some instances τ_{BK} is so crucial in shaping the bursting trajectories whilst in others it has virtually no influence.

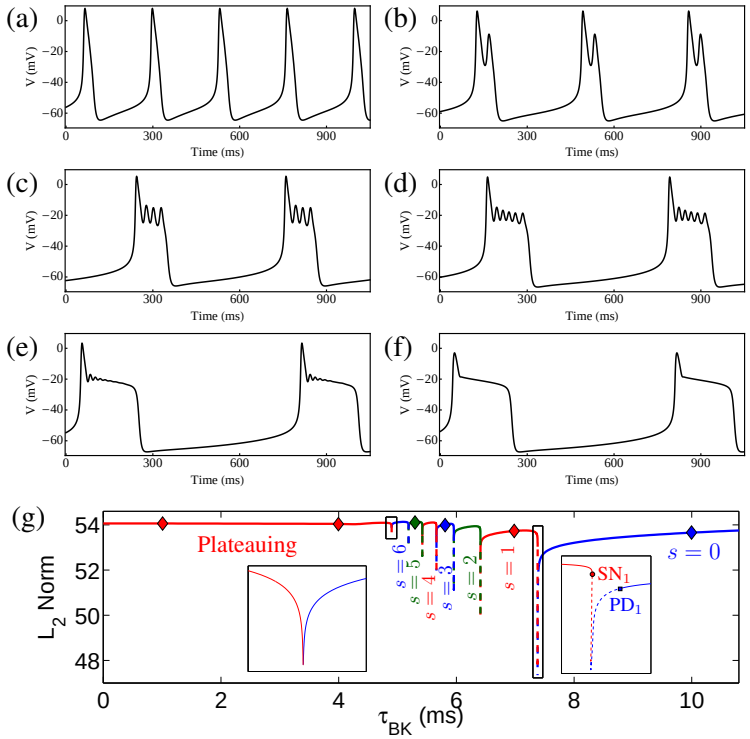

Figure 2: (a) $\tau_{BK} = 10$ ms, (b) $\tau_{BK} = 7$ ms, (c) $\tau_{BK} = 5.8$ ms, (d) $\tau_{BK} = 5.3$ ms, (e) $\tau_{BK} = 4$ ms and (f) $\tau_{BK} = 1$ ms. (g) Bifurcation structure with respect to τ_{BK} for $C_m = 5$ pF and $g_{BK} = 0.5$ nS.

3 Geometric Singular Perturbation Analysis

Geometric singular perturbation theory (GSPT) [4, 5] is an analytic technique for slow/fast systems that combines asymptotic theory with dynamical systems techniques. We first show that (1) is a slow/fast problem. By introducing dimensionless time variable $t = k_t t_s$ and suitable scalings, we rewrite (1) as

$$\begin{aligned} \varepsilon_1 \frac{dV}{dt_s} = \frac{C_m}{k_t g_{\text{ref}}} \frac{dV}{dt_s} &= f_1(V, b, n, c), \\ \varepsilon_2 \frac{db}{dt_s} = \frac{\tau_{BK}}{k_t} \frac{db}{dt_s} &= b_\infty(V) - b \equiv f_2(V, b), \\ \frac{dn}{dt_s} &= \frac{k_t}{\tau_n} \left(n_\infty(V) - n\right) \equiv g_1(V, n), \\ \frac{dc}{dt_s} &= -k_t f_c k_c \left(\frac{\alpha}{k_c} I_{Ca} + c\right) \equiv g_2(V, c), \end{aligned} \tag{2}$$

where $k_t = \tau_n$ is a reference time scale, $g_{\text{ref}} = \mathcal{O}(1)$ nS is a typical conductance scale and

$$f_1(V, b, n, c) := -g_{\text{ref}}^{-1} \left(I_{Ca} + I_{BK} + I_K + I_{SK} + I_L\right).$$

From (2), V has time constant $C_m/g_{\text{ref}} = 1$ ms for $C_m = 5$ pF and $g_{\text{ref}} = 5$ nS. Meanwhile, b has timescale $\tau_{BK} = 5$ ms. The gating variable n is slower with timescale $\tau_n = 30$ ms, whilst c is substantially slower with timescale $(f_c k_c)^{-1} > 800$ ms. To formalize the timescale separation, we introduce the small parameters $\varepsilon_1 \equiv C_m/(k_t g_{\text{ref}})$ and $\varepsilon_2 \equiv \tau_{BK}/k_t$, which measure the relative speeds of V and b to n, respectively. Although it is not clear whether or not V and b operate on similar timescales, it is clear that both V and b are substantially faster than (n, c). Thus, (2) is singularly perturbed with fast variables (V, b), slow variables (n, c) and small parameters $(\varepsilon_1, \varepsilon_2)$.

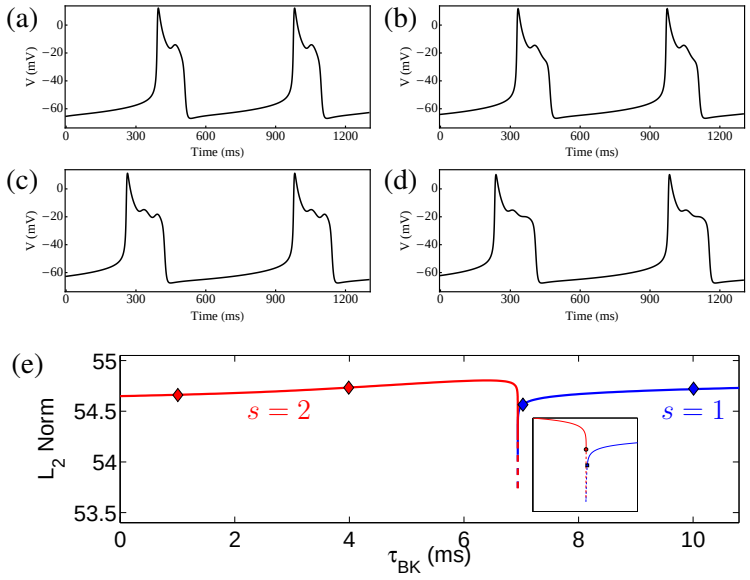

Figure 3: Time traces and bifurcation structure of (1) for $C_m = 5$ pF and $g_{BK} = 0.1$ nS. In (a), $\tau_{BK} = 10$ ms, (b) $\tau_{BK} = 7$ ms, (c) $\tau_{BK} = 4$ ms and (d) $\tau_{BK} = 1$ ms.

System (2) is currently described over the slow timescale t_s. An equivalent description of the dynamics can be obtained by rescaling time ($t_s = \varepsilon_2\, t_f$) to give:

$$\begin{aligned}
\frac{dV}{dt_f} &= \frac{\varepsilon_2}{\varepsilon_1} f_1(V, b, n, c), \\
\frac{db}{dt_f} &= f_2(V, b), \\
\frac{dn}{dt_f} &= \varepsilon_2\, g_1(V, n), \\
\frac{dc}{dt_f} &= \varepsilon_2\, g_2(V, c).
\end{aligned} \tag{3}$$

The next step is to take the singular limit to decompose (1) into simpler subsystems. The presence of two small parameters naturally leads to the question of which limit to take. We make the *a priori* assumption that V and b vary on similar timescales. As such, we take the double singular limit under the stipulation that the relative speeds of V and b remain comparable. Formally, we assume that

$$\lim_{(\varepsilon_1, \varepsilon_2) \to (0,0)} \frac{\varepsilon_2}{\varepsilon_1} = r, \tag{4}$$

where $r = \mathcal{O}(1)$ so that $\varepsilon_2 = r\, \varepsilon_1$. The (double) singular limit $\varepsilon_2 \to 0$ (and hence $\varepsilon_1 \to 0$) in (3) leads to the 2D *layer problem*:

$$\begin{aligned}
\frac{dV}{dt_f} &= r f_1(V, b, n, c), \\
\frac{db}{dt_f} &= f_2(V, b),
\end{aligned} \tag{5}$$

where n and c are parameters. The singular limit $\varepsilon_2 \to 0$ in (2) gives the 2D *reduced problem*:

$$\begin{aligned}
0 &= f_1(V, b, n, c), \\
0 &= f_2(V, b), \\
\frac{dn}{dt_s} &= g_1(V, n), \\
\frac{dc}{dt_s} &= g_2(V, c).
\end{aligned} \tag{6}$$

The idea of GSPT is to combine the information from the 2D layer problem and the 2D reduced problem in order to gain insight into the original 4D cell model (1).

3.1 The Layer Problem

The set of equilibria for the layer problem is a surface called the *critical manifold*:

$$S := \left\{(V, b, n, c) \in \mathbb{R}^4 : f_1(V, b, n, c) = f_2(V, b) = 0\right\}. \tag{7}$$

Since n and b enter linearly into f_1 and f_2, respectively, we can obtain a graph representation of S:

$$b = b_\infty(V), \quad n = -\frac{1}{g_K}\left(g_{Ca} m_\infty(V)\frac{V-V_{Ca}}{V-V_K} + g_{BK} b_\infty(V) + g_{SK} s_\infty(c) + g_L \frac{V-V_L}{V-V_K}\right). \tag{8}$$

The critical manifold S is typically a folded surface. The fold curves, L, of S are the set of points where the layer problem undergoes a saddle-node bifurcation:

$$L := \{(V, b, n, c) \in S : \det J_r = f_{1V} f_{2b} - f_{1b} f_{2V} = 0\}, \tag{9}$$

where J_r is the Jacobian of (5). These fold curves divide S into attracting sheets, S^a, and repelling sheets, S^r, where the notions of attraction and repulsion come from a linear stability analysis of (5).

The fold curves are of interest because they are points where Fenichel theory [4, 5] breaks down. More generally, Fenichel theory breaks down in the neighbourhood of bifurcations of (5). Usually, the interesting dynamics are localized around these non-hyperbolic regions. Another way that Fenichel theory can break down is via a Hopf bifurcation of (5). The Hopf curves, H, of (5) are given by:

$$H := \{(V, b, n, c) \in S : \operatorname{tr} J_r = r f_{1V} + f_{2b} = 0\}. \tag{10}$$

For normally hyperbolic critical manifolds (i.e. the eigenvalues of (5) along S are uniformly bounded away from the imaginary axis), Fenichel theory guarantees the persistence of locally invariant slow manifolds $S_{(\varepsilon_1,\varepsilon_2)}$ of the fully perturbed problem (2) for sufficiently small perturbations.

According to (5), most initial conditions starting away from S will be drawn into one of the attracting sheets of S. Once the trajectory is on S, (5) predicts trivial dynamics. At this point, the slow processes dominate and the layer flow is no longer a suitable approximation of the dynamics. As such, we must switch viewpoints and consider the slow dynamics via the reduced system.

3.2 The Reduced Problem

The reduced problem is a differential-algebraic system, consisting of algebraic equations that constrain the dynamics to S and differential equations that describe the slow motions along S. The restriction of the flow of (2) to the invariant slow manifolds $S_{(\varepsilon_1,\varepsilon_2)}$ is a small smooth perturbation of the slow flow along S.

To analyze the flow on a manifold, one must typically look at the flow in various coordinate charts. To obtain evolution equations in all coordinate charts for the reduced problem (6), we take a total time derivative of the algebraic constraints and rearrange to obtain:

$$\begin{pmatrix} -J & \mathbb{O} \\ \mathbb{O} & \mathbb{I}_2 \end{pmatrix} \frac{d}{dt_s}\begin{pmatrix} V \\ b \\ n \\ c \end{pmatrix} = \begin{pmatrix} f_{1n} g_1 + f_{1c} g_2 \\ 0 \\ g_1 \\ g_2 \end{pmatrix}, \tag{11}$$

where $J = J_r|_{r=1}$, $\mathbb{O}$ is the 2×2 zero matrix and $\mathbb{I}_2$ is the 2×2 identity matrix. Multiplying both sides by the 4×4 matrix $\operatorname{diag}(-\operatorname{adj}(J), \mathbb{I}_2)$, where $\operatorname{adj}(J)$ is the adjoint of J, leads to:

$$\begin{pmatrix} (\det J)\,\mathbb{I}_2 & \mathbb{O} \\ \mathbb{O} & \mathbb{I}_2 \end{pmatrix} \frac{d}{dt_s}\begin{pmatrix} V \\ b \\ n \\ c \end{pmatrix} = \begin{pmatrix} -f_{2b}\,(f_{1n} g_1 + f_{1c} g_2) \\ f_{2V}\,(f_{1n} g_1 + f_{1c} g_2) \\ g_1 \\ g_2 \end{pmatrix}, \tag{12}$$

which describes the flow of the reduced problem on S in the coordinates (V, b, n, c). Since S has a graph representation (8), we can use a single coordinate chart to describe the dynamics of (6):

$$\begin{aligned} \det J \frac{dV}{dt_s} &= -f_{2b}\left(f_{1n}g_1 + f_{1c}g_2\right), \\ \frac{dc}{dt_s} &= g_2, \end{aligned} \tag{13}$$

where b and n are now specified by (8). The projection of the reduced system (13) highlights an important fact: the reduced system is singular at the fold curves L. This singular term can be removed by a time rescaling ($dt_s = \det J \, dt_d$) to give the *desingularized system*:

$$\begin{aligned} \frac{dV}{dt_d} &= -f_{2b}\left(f_{1n}g_1 + f_{1c}g_2\right) \equiv F(V, c), \\ \frac{dc}{dt_d} &= \det J \, g_2. \end{aligned} \tag{14}$$

Note that in regions where $\det J < 0$, the time rescaling reverses the orientation of trajectories.

The desingularized system possesses special equilibria called *folded singularities* [12]. Folded singularities, M, are points on the fold curve where F vanishes:

$$M := \{(V, b, n, c) \in L : F = 0\}. \tag{15}$$

In the desingularized system, M is a set of equilibria. In the reduced system (13), folded singularities are points where both sides of the V-equation vanish. This means there is potentially a cancellation of a simple zero, i.e. dV/dt_s is finite and non-zero at a folded singularity. This allows trajectories to cross L in finite time and move from S^a to S^r. Such solutions are called *singular canards* and their persistence under small perturbations gives rise to complex dynamics [1]. There are three generic types of folded singularities (based on the eigenvalues of the linearization of (14)): folded saddles, folded nodes, and folded foci. Folded nodes are of particular interest.

4 Canard- and Hopf-Induced Bursts

Two distinct mechanisms for bursting are: canard dynamics and slow passage through a dynamic Hopf bifurcation [2]. Canard dynamics are associated with the slow subsystem and have been found in other neuroendocrine cell models to be the progenitor for the bursting behaviour. The slow passage through a dynamic Hopf bifurcation can be observed when there is a Hopf bifurcation in the fast subsystem that is unrelated to equilibria of the full system.

4.1 Canard Dynamics

Folded nodes can lead to counter-intuitive behaviour due to the indeterminate form for the V-equation in (13). More specifically, it is possible for trajectories that reach the folded singularity to pass through it with finite speed. This potential for trajectories to tunnel through the fold is the linchpin of the argument for the burst generating mechanism in *canard-induced MMOs*. Here, we illustrate how this tunnelling behaviour can lead to the small oscillations of a burst.

Figure 4 shows a singular orbit construction in which there is a folded node on the upper fold curve L^+. Associated to the folded node is a subset of the attracting manifold S^a called the *funnel* of the folded node (grey shaded). The funnel is bounded by L^+ and by the *strong canard* γ_0, which is the unique trajectory tangent to the strong eigendirection of the folded node. Every trajectory that lands inside the funnel region is inevitably drawn into the folded node and is thus a singular canard.

According to canard theory, such a singular periodic orbit will perturb to a bursting orbit for sufficiently small perturbations $\mathcal{O}(\varepsilon_2)$. Moreover, the SAOs occur in a neighbourhood of the folded

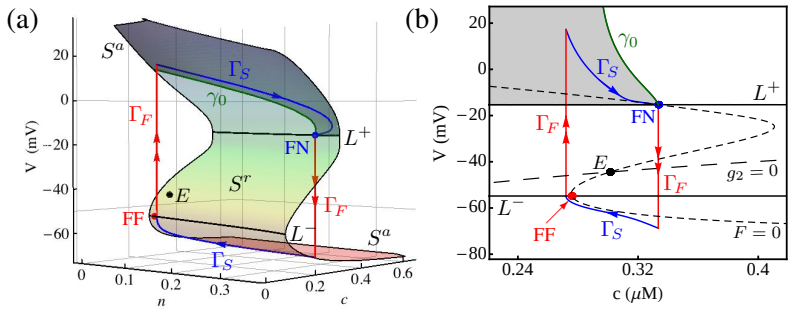

Figure 4: Singular orbit construction in the case of canard-induced bursts for $g_{BK} = 0.1$ nS and $r = 1$. There is a folded node on L^+ and the fast up-jump of the singular orbit returns it to the funnel (shaded region).

node (Figure 5). Furthermore, the maximal amplitude of these SAOs is $\mathcal{O}(\sqrt{\varepsilon_2})$. The rotational behaviour in a neighbourhood of the folded node arises from geometric properties of invariant slow manifolds. We refer to [1, 12] for details. Figure 5 shows how the singular canard orbits perturb to bursts for fixed ratio r and various perturbations ε_2.

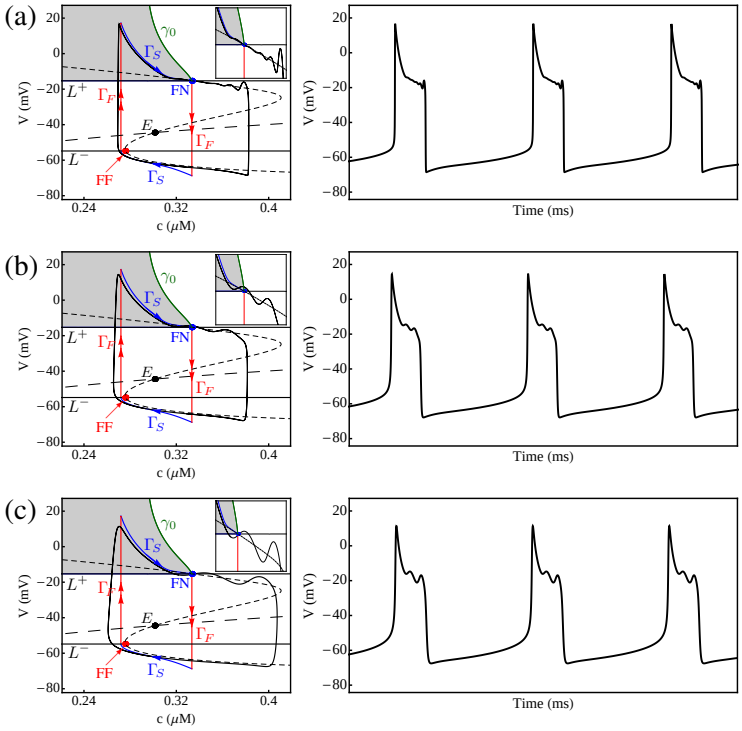

Figure 5: Canard-induced bursts for $g_{BK} = 0.1$ nS, $r = 1$ and (a) $C_m = 0.5$ pF, $\tau_{BK} = 0.5$ ms (b) $C_m = 2$ pF, $\tau_{BK} = 2$ ms and (c) $C_m = 5$ pF, $\tau_{BK} = 5$ ms (cf. Figure 4). The left panels show the singular ($\Gamma_F \cup \Gamma_S$) and non-singular orbits in the (V, c) plane. The right panels show the associated time courses.

4.2 Slow Passage Through A Dynamic Hopf Bifurcation

Canard-induced bursts arise from the canard dynamics associated with folded node singularities in (6) and provide one burst generating mechanism. Another mechanism for bursting is the slow passage through a dynamic Hopf bifurcation [6]. The major difference from the canard case is that there is now a curve of (subcritical) Hopf bifurcations H on S.

In Figure 6, it is clear that H occurs at a more depolarized voltage level than L^+. This means S^r is now enclosed by H and L^-. Since the upper attracting sheet of S terminates at H, the corresponding singular orbit must jump at H, where the stability changes. In the full system trajectory however,

there is a substantial delay before the trajectory oscillates and jumps to the lower attracting manifold (Figure 6(a)). This delay is mainly observed for small perturbations $\mathcal{O}(\varepsilon_2)$. For larger perturbations, the delay is less substantial and the SAOs are observed on both sides of the Hopf curve.

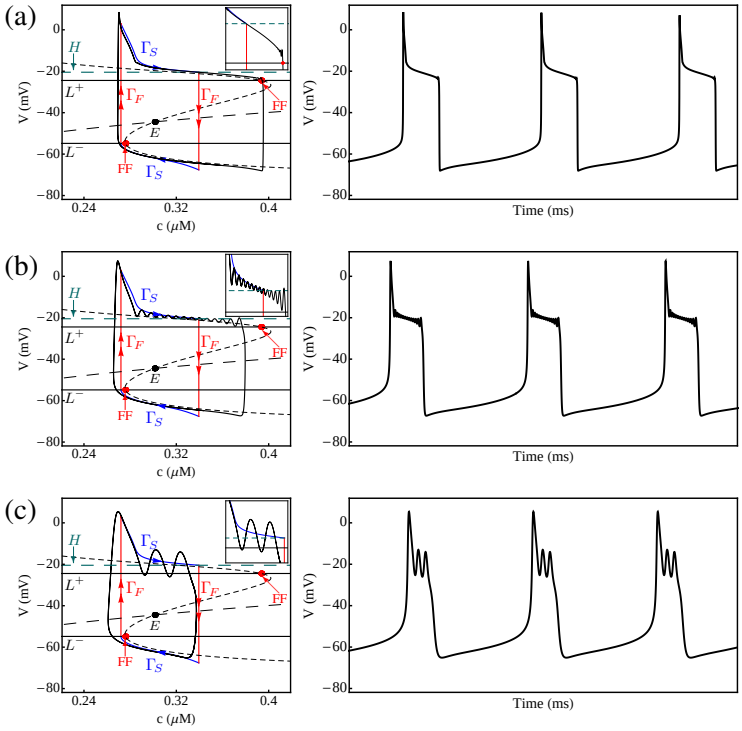

Figure 6: Hopf-induced MMOs for $g_{BK} = 0.5$ nS, $r = 1.2$ and (a) $C_m = 0.5$ pF, $\tau_{BK} = 0.6$ ms (b) $C_m = 2$ pF, $\tau_{BK} = 2.4$ ms and (c) $C_m = 5$ pF, $\tau_{BK} = 6$ ms. Note: C_m and τ_{BK} are chosen so that $r = 1.2$.

The flow of (1) in a neighbourhood of H can be understood in very simple terms. For $\varepsilon_2 = 0$, (n, c) are fixed parameters. For $\varepsilon_2 \neq 0$, n and c are slow variables that drift through the vicinity of H. As the trajectory approaches H from S^a, the eigenvalues λ of (5) are complex with (increasing) negative real part. Exponential contraction of the system means that the trajectories become exponentially close to S^a. As the trajectory passes H over to S^r, $\mathrm{Re}\,\lambda$ crosses zero and becomes positive. However, the trajectories are not immediately repulsed. The expansion required to counteract the accumulative contraction on S^a is the cause for the observed delay. The slower the trajectories drift through the Hopf H, the longer the delay. Conversely, if ε_2 increases, the passage through H speeds up. Consequently, trajectories spend less time on S^a and hence less time is required on S^r to counterbalance the contraction.

The amplitude and number of SAOs is related to the size of the perturbation (i.e. to the amount of time spent in a neighbourhood of H). For small perturbations, the passage through H is slow and the trajectories are exponentially attracted to S^a. As such, the small oscillations are only visible when the repulsion along S^r overwhelms the accumulative contraction on S^a and the trajectory jumps away. When ε_2 is increased, the attraction to S^a is weaker and the oscillatory behaviour is easier to observe. Moreover, $\mathrm{Re}\,\lambda$ increases through zero. As such, the SAOs have decreasing amplitude on S^a and increasing amplitude on S^r.

4.3 Damped Oscillations & Plateauing

The amount and type of contraction along the slow flow on S^a shapes the trajectories. When the eigenvalues λ of (5) along slow orbit segments on S^a are real, trajectories are attracted (or repelled) along nodes of (5). When λ is complex, the attraction (or repulsion) occurs along foci of (5), resulting in oscillatory behaviour in the full system trajectory. A key parameter that influences the amount and

type of contraction along S^a is the ratio r of fast timescales. Figure 7 shows the effect of varying r on the bursts[1].

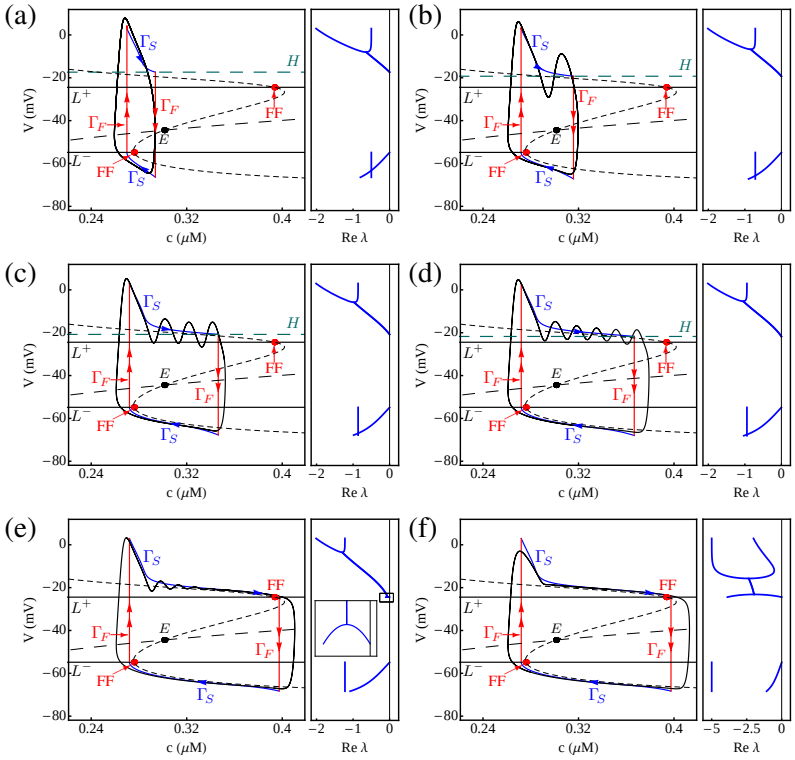

Figure 7: The eigenvalues of (5) along Γ_S regulates the type of bursting pattern. Singular and non-singular orbits are shown for $C_m = 5$ pF, $g_{BK} = 0.5$ nS and (a) $\tau_{BK} = 10$ ms ($r = 2$), (b) $\tau_{BK} = 7$ ms ($r = 1.4$), (c) $\tau_{BK} = 5.8$ ms ($r = 1.16$), (d) $\tau_{BK} = 5.3$ ms ($r = 1.06$), (e) $\tau_{BK} = 4$ ms ($r = 0.8$) and (f) $\tau_{BK} = 1$ ms ($r = 0.2$). The inset in (e) shows the second degenerate node and switch from complex to real eigenvalues. Note the shifted scale on Re λ in (f). The parameters were chosen to correspond to those in Figure 2.

Each panel of Figure 7 shows 2 plots. In the main plot, the singular orbit (red and blue) together with the full system trajectory Γ (black) are shown. In the adjacent plot, $\mathrm{Re}\,\lambda$ evaluated along the slow orbit segment Γ_S on S^a is shown. In panel (a), the eigenvalues on the stable top sheet are initially real and negative. As the reduced flow brings the trajectory towards the Hopf curve, λ becomes complex. However, this region of complex eigenvalues is short lived. As a result, Γ has insufficient time to oscillate and we observe a spike. In panel (b), the region of complex λ is more extensive, which provides Γ just enough time to perform one small oscillation before jumping away. As r is decreased, the region of complex eigenvalues becomes more extensive (panels (c) and (d)), resulting in more SAOs.

As r decreases further, H moves closer to L^+. Eventually, H and L^+ coalesce resulting in a double zero eigenvalue, i.e. a Bogdanov-Takens (BT) bifurcation, of (5). Before the BT bifurcation when S^r is enclosed by H and L^-, the eigenvalues of (5) along Γ_S are initially real (at the landing point after the fast up-jump). The slow flow moves the singular orbit through a degenerate node of (5) and λ becomes complex and remains so until the singular orbit reaches the Hopf curve. In the full system trajectory, this is seen as oscillatory behaviour with decreasing amplitude.

After the BT bifurcation, H disappears and S^r is enclosed by L^+ and L^-. The eigenvalues of (5) along Γ_S are initially real and the slow flow moves the orbit through a degenerate node of (5) where the eigenvalues become complex. The difference this time is that Γ_S passes through another degenerate node and λ becomes real once again (panels (e) and (f)). This second degenerate node

[1]Variations in r (which only appears in the fast subsystem) have no effect on the singular canards which are associated with the slow subsystem.

is born at the BT bifurcation and moves away from L^+ to more depolarized voltage levels as r is decreased. Γ_S on the upper sheet of S^a can be decomposed into 3 parts:

1. An 'upper' part (between the landing point of the fast up-jump and the first degenerate node of (5)): manifests in the full system as a monotone decrease to more hyperpolarized V.
2. A 'middle' part (between the degenerate nodes): corresponds to decaying oscillations.
3. A 'lower' segment (between the second degenerate node and L^+): corresponds to a plateau phase of the full system orbit, where there is only monotone contraction and the SAOs die out.

Smaller ratios r move the second degenerate node to more depolarized V levels, which causes greater damping of the SAOs (compare panels (e) and (f)). Thus, variations in the ratio r can convert the full system trajectory from spiking to bursting to plateauing.

5 Experimental Work

We have demonstrated the existence of canard- and Hopf-induced bursts in (1). The question is whether or not they are observed experimentally. A simple test to distinguish between canard- and Hopf-induced bursts is to inject artificial BK current (via dynamic clamp) into a cell and vary τ_{BK}. Based on our analysis, we expect (for fixed C_m) the canard-induced bursts to have weak response to τ_{BK} variations, whilst the Hopf-induced bursts should have extreme sensitivity to τ_{BK} variations.

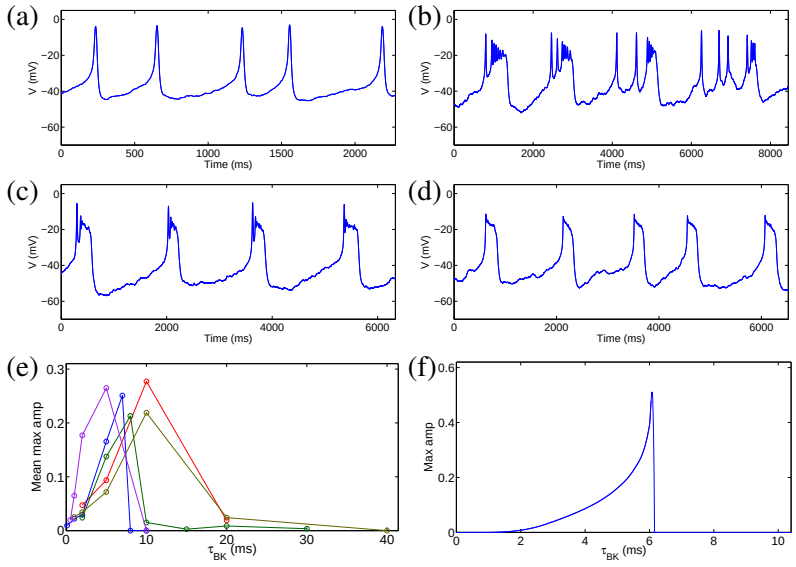

Figure 8: Effect of τ_{BK} variations in dynamic clamp experiments. (a) $\tau_{BK} = 10$ ms: the cell is spiking. (b), $\tau_{BK} = 7$ ms: the time course is a mixture of spikes and bursts. (c), $\tau_{BK} = 5$ ms: the cell is bursting. (d), $\tau_{BK} = 2$ ms: the electrical activity consists of plateau patterns. (e) Summary of the behaviour of the amplitude of the SAOs in five different cells. The g_{BK} values for the red, blue, green, olive and purple curves are $g_{BK} = 0.5, 1.6, 2, 0.5, 1$ nS, respectively. The blue curve ($g_{BK} = 1.6$ nS) corresponds to the cell in panels (a) to (d). Panel (f) shows the same figure for the model (1) with $C_m = 5$ pF, $g_K = 3.2$ nS and $g_{BK} = 0.5$ nS.

The dynamic clamp technique is an electrophysiological technique whereby a current, computed from mathematical models, is injected into a cell to simulate dynamic processes [7]. The current of interest in our case is $I_{BK} = g_{BK} b(V - V_K)$. In order to update the BK activation variable b and driving force $V - V_K$, information on the voltage V is required. In the dynamic clamp technique, rather than using a model for V, the voltage is recorded in real time from the cell and used in calculations. Thus, the computer calculates the model I_{BK} using V from the cell, then injects the model current into the cell. This two-way interaction is done rapidly, at average time steps of 54 μs.

In Figure 8, we show evidence for Hopf-induced bursts in pituitary cells. Panels (a) to (d) show the effect of varying τ_{BK} for fixed g_{BK}. For BK current injected with τ_{BK} large, the cell is spiking

(panel (a)). By decreasing τ_{BK}, we observe bursting interspersed with the spiking activity (panel (b)). Further decreasing τ_{BK} reliably converts the electrical activity to bursting (panel (c)). Moreover, the amplitude of the SAOs decreases with τ_{BK}. For sufficiently small τ_{BK}, the small oscillations are virtually non-existent and the electrical activity is plateauing (panel (d)). These observations are consistent with the prediction that for Hopf-induced bursts, decreasing τ_{BK} switches the activity from spiking to bursting to plateauing (Figure 7).

Figures 8 (e) and (f) quantify how changing τ_{BK} affects the electrical activity in the dynamic clamp experiments and in (1), respectively. We refer to [11] for details. The main result is that the model predicts the trends observed experimentally. Namely, that fast BK activation generates bursting with small oscillations that decrease in amplitude as τ_{BK} is decreased. The dynamic clamp data provides direct evidence for the Hopf mechanism. Evidence for the canard-induced MMOs is more elusive.

References

[1] M. Brøns, M. Krupa and M. Wechselberger, *Mixed mode oscillations due to the generalized canard phenomenon*, Fields Institute Communications, **49** (2006), 39–63.

[2] M. Desroches, J. Guckenheimer, B. Krauskopf, C. Kuehn, H. M. Osinga and M. Wechselberger, *Mixed-mode oscillations with multiple time scales*, SIAM Review, **54** (2012), 211–288.

[3] E. J. Doedel, A. R. Champneys, T. F. Fairgrieve, Y. A. Kuznetsov, K. E. Oldeman, R. C. Paffenroth, B. Sanstede, X. J. Wang and C. Zhang, *AUTO-07P: Continuation and bifurcation software for ordinary differential equations*, Available from: http://cmvl.cs.concordia.ca/

[4] N. Fenichel, *Geometric singular perturbation theory for ordinary differential equations*, Journal of Differential Equations, **31** (1979), 53–98.

[5] C. K. R. T. Jones, *Geometric singular perturbation theory*, in "Dynamical Systems" (ed. R. Johnson), Lecture Notes in Mathematics, Springer, New York (1995), 44–120.

[6] A. Neishtadt, *On stability loss delay for dynamical bifurcations*, Discr. Cont. Dyn. Syst. Ser. S, **2** (2009), pp. 897–909.

[7] A. A. Sharp, M. B. O' Neil, L. F. Abbott and E. Marder, *Dynamic clamp – computer-generated conductances in real neurons*, Journal of Neurophysiology, **69** (1993), 992–995.

[8] S. S. Stojilkovic, H. Zemkova, and F. Van Goor, *Biophysical basis of pituitary cell type-specific Ca^{2+} signaling-secretion coupling*, Trends In Endocrinology and Metabolism, **16** (2005), 152–159.

[9] P. Szmolyan and M. Wechselberger, *Relaxation oscillations in $\mathbb{R}^3$*, Journal of Differential Equations, **200** (2004), 69–104.

[10] J. Tabak, M. Tomaiuolo, A. E. Gonzalez-Iglesias, L.S. Milescu and R. Bertram, *Fast-activating voltage- and calcium-dependent potassium (BK) conductance promotes bursting in pituitary cells: a dynamic clamp study*, Journal of Neuroscience, **31** (2011), 16855–16863.

[11] T. Vo, J. Tabak, R. Bertram and M. Wechselberger, *A geometric understanding of how fast activating potassium channels promote bursting in pituitary cells*, Journal of Computational Neuroscience, **36** (2014), 259–278.

[12] M. Wechselberger, *Existence and bifurcation of canards in $\mathbb{R}^3$ in the case of a folded node*, SIAM Journal of Dynamic Systems, **4** (2005), 101–139.